Acta Materialia 228 (2022) 117776

Contents lists available at ScienceDirect

Acta Materialia

journal homepage: www.elsevier.com/locate/actamat

Full length article

Structural properties of single-walled carbon nanotubes under extreme dynamic pressures

Bo Li[a,1], Shufeng Li[a,*], Kaiyuan Shi[b,c,1], Xin Zhang[a], Shenghui Yang[a], Deng Pan[a], Lei Liu[a], Yanli Nan[d], Xiang Zhu[e], Xiaolong Song[f], Lei Su[b,c,*], Guoqiang Yang[b,*]

[a] School of Materials Science and Engineering, Xi'an University of Technology, Xi'an, 710048, P.R.China
[b] Key Laboratory of Photochemistry, Institute of Chemistry, University of Chinese Academy of Sciences, Chinese Academy of Sciences, Beijing, 100190, P.R.China
[c] Center for High Pressure Science and Technology Advanced Research, Beijing 100094, P.R.China
[d] School of Material Science and Engineering, Shaanxi Key Laboratory of Nano Materials and Technology, Xi'an University of Architecture and Technology, Xi'an, 710055, P.R.China
[e] Center for High Pressure Science and Technology Research, Zhengzhou University of Light Industry, Zhengzhou, 450002, P.R.China
[f] State Key Laboratory for Mechanical Behavior of Materials, School of Materials Science and Engineering, Xi'an Jiaotong University, Xi'an, 710049, P.R.China

ARTICLE INFO

Article history:
Received 17 June 2021
Revised 7 February 2022
Accepted 18 February 2022
Available online 19 February 2022

Keywords:
Carbon nanotubes
High pressure
Compression rate
Raman spectroscopy
Structural phase transition

ABSTRACT

The structural behaviors of single-walled carbon nanotubes (SWNTs) along the radial direction are critical to the cross-sectional phase transition, elastic recovery, and band structure engineering. Previous static pressure studies have established a clear picture on the structural behaviors of SWNTs that governed by the Lévy-Carrier law. But when the pressurization becomes dynamic, there lacks a fundamental understanding of the structural properties of SWNTs along the radial direction. Here, different from static (< 1 GPa/s) and shock compression (> 10^7 GPa/s), we gain new insights on the phase transition, recovery dynamics and energy dissipation of SWNT bundles with a median diameter of d_t ~1.4 and ~0.8 nm under *modest* dynamic pressures in two common pressure mediums (4:1 methanol-ethanol mixture, silicone oil). Upon single ramp compression (ramp rate in an order of magnitude of ~10–10^3 GPa/s), the lineshape and intensity changes of Raman spectra induced by the dynamic effect of hydrostatic stress are commonly observed, suggesting different structural behaviors compared with static pressure results. Unexpectedly, the pressure-induced defects are not found in cyclic ramp compressions up to 10^5 cycles, showing high structural stability to dynamic loading. The corresponding recovery dynamics and energy dissipation mechanism of SWNTs under varying dynamic conditions are also discussed. By analyzing the shear strain potential, distinct dynamic effects of hydrostatic pressure on the SWNTs in two pressure mediums are quantitatively unveiled.

1. Introduction

Pressure modulation of the radial structure and property of single-walled carbon nanotubes (SWNTs) offers interesting perspectives for mechanical resilience and energy storage [1], structural phase transition [2,3], semiconductor-metal transition [4,5], and strain-dependent band structure engineering [6]. One of the most important pressure effects on SWNTs is pressure-induced geometrical deformation of its cross section. This effect under static high pressure has been studied by numerous theoretical and experimental efforts. Continuum elastic mechanics predicts that radial collapse pressure, P_c, depends on nanotube diameter d_t, following the Lévy-Carrier law, $P_c \sim d_t^{-3}$ [7,8], or other power law forms [9,10]. Recently, new insights on collapse phase diagram of CNTs have been gained at multiscale levels by Magnin et al. [11]. Large enough d_t (>2.5 nm) will lead to structural collapse/flattening induced by van der Waals (vdW) interaction at ambient pressure [12,13]. Experimentally, a number of static pressure works suggest, for example, a structural phase transition at P_c ~2 GPa for a commonly used (10,10) nanotube with d_t ~1.35 nm according to a complete quenching (disappearance) of radial breathing mode (RBM) [14,15], or the frequency anomaly of squash mode (ω_{SM}<100 cm^{-1}) [16]. At higher pressure (>10 GPa),

* Corresponding author.
E-mail addresses: shufengli@xaut.edu.cn (S. Li), leisu2050@iccas.ac.cn (L. Su), gqyang@iccas.ac.cn (G. Yang).
[1] These authors contribute equally to this work.

https://doi.org/10.1016/j.actamat.2022.117776
1359-6454/

more structural transitions were also reported according to the frequency shift anomaly or plateau-like behavior of tangential G mode [17–19]. Overall, previous results have promoted a picture of structural transition of SWNTs under static pressure, that is, following a sequence of circular, polygonal (for bundles), oval, peanut-like cross-sectional shapes as pressure increases. In addition, high resilience for the middle (1 nm < d_t < 2 nm) and small (< 1 nm) SWNTs were also observed after radial deformation. Yet, unfortunately, structural defects or lattice disorder would simultaneously generate even in elastic deformation, and the recovery might be slow [19–21]. Compared with static process (isothermal), *modest* dynamic pressure, an intermediate state between isothermal and shockwave adiabatic process, not only prevails in natural evolution, but also in condensed matter physics and materials science [22–24]. As a nascent field, new insights have been gained in phase transition kinetics and metastable phase research, e.g., water [25,26]. So far there has been a relatively small number of studies regarding dynamic structural and mechanical properties of SWNTs, most of which were based on micropillar samples made by vertically aligned carbon nanotube (VACNT) arrays, and thus obtaining an extrinsic, collective property of massive nanotubes [27–30]. Moreover, such cyclic or fatigue measurements were performed by uniaxial stress along the axial direction of nanotubes. It was found that its viscoelastic, strain-rate-dependent recovery and energy dissipation mechanism is dominated by the synergistic contribution of axial C–C stiffness, radial elasticity and preexisting defects. For example, a recent report on fatigue behavior of ultralong SWNTs showed that the fatigue resistance depends on the creation of its first defect [31]. With the fast growing R&D of SWNT-based applications, e.g., artificial muscles [32], there is still an urgent need to explore the intrinsic, radial response of SWNTs to dynamic load, and some fundamental questions are expected to be answered: 1) Are radial structural and vibrational properties of SWNTs compression-rate-dependent? 2) Does the triangular lattice of SWNTs deteriorate, or, how pressure-induced defects behave during varying dynamic compressions?

In this work, we scrutinize the main vibrational modes (RBM, D and G) of the SWNTs with two median diameters, d_t ~1.4 and ~0.8 nm, under varying dynamic conditions by using dynamic moissanite/diamond anvil cell (d-MAC/DAC) coupled with in situ time-resolved Raman spectroscopy (Fig. 1). Two common pressure transmitting mediums (PTM), 4:1 methanol-ethanol mixture and silicone oil, were used to probe the influence of hydrostaticity. Prior to the dynamic experiments, we also performed static pressure tests for comparison. Our results show that there does exist the dynamic effect of hydrostatic pressure which varies with the peak pressure and ramp rate. Moreover, the structural behaviors of SWNTs have been investigated under cyclic ramp compressions with varying conditions. We particularly focus on the recovery dynamics and energy dissipation of SWNTs under single and cyclic ramp compressions. The dynamic effect on pressure-induced volume deformation of SWNTs is analyzed theoretically and can be well explained by the introduction of shear strain. In each section, the possible influence of PTM is also concerned.

2. Materials and methods

Sample information. Two commercial high-quality SWNT bundles with nanotube content ≥95% are used in this work (see Fig. S1 in supporting information, SI). The (6,5) enriched SWNTs with a small diameter distribution (~ 0.8 ± 0.1 nm) and a median length of ~1 μm, is produced by CoMoCAT method (773,735#, Sigma-Aldrich). The second sample exhibits a diameter range of 1–2 nm and a wide length distribution of 5–30 μm, is produced by floating catalytic method (C140992#, Aladdin). Raman spectroscopy shows that two samples are highly homogeneous, and the large d_t sample is estimated to be ~1.35–1.77 nm with a high contribution from those tubes centered ~1.42 nm, according to the inverse proportion of RBM frequency to tube diameter for a bundle, $\omega_{RBM} = 234/d + 10$ [33]. The possible chirality can correspond to either (12,12) armchair tubes or (13,11), (12,9), (11,10) chiral tubes, or any other appropriate combination of (n, m). At ambient condition, the tangential G band consists of three (1563, 1573 and 1594 cm^{-1}) and four (1502, 1525, 1544 and 1594 cm^{-1}) symmetric Lorentzian subpeaks for the ~1.4 and ~0.8 nm samples, respectively (Fig. S2).

Dynamic and static pressure experiments. Symmetric moissanite and diamond anvil cells (MAC/DAC) with 300 μm anvil culets were used for different purposes. The SWNTs powder was loaded into the sample chamber with a diameter of ~150 μm in a stainless-steel gasket with an indented thickness of ~70 μm. A small piece of ruby was added as pressure marker according to the redshift of R1 line. Silicone oil and 4:1 methanol-ethanol mixture was used to probe the influence from the PTM. In particular, silicone oil was only used for cyclic ramp compression due to the volatility of methanol-ethanol mixture. The dynamic pressure is realized by the piezoelectric (PE) actuator and the PE drive is taken by PE power supply and is controlled by arbitrary function generator [22]. In this work, we utilized d-MAC/d-DAC that incorporates three PE actuators into a MAC/DAC for controllable dynamic loading (Fig. 1a). More information about this novel dynamic loading device is available in a recent paper [34]. The modulation parameters of dynamic load could be precisely controlled by adjusting the waveform of input signals to PE actuators. In fact, to operate a dynamic test, three modulation parameters usually need to be set up, that is, the pressure of precompression (P_{pre}), peak pressure (P_{max}), and ramp time (Δt), as shown in Fig. 1b. The ramp (compression) rate can be obtained by these three quantities (see the inset of Fig. 1b). For cyclic ramp compression, another two parameters are added, namely, pressure oscillation ($P_{max}-P_{min}$), and cycle number. It should be noted that the P_{min} is an uncontrollable parameter that depends on the elastic property of the gasket. On the other hand, to describe the extreme degree of dynamic process, two key parameters, i.e., peak pressure and ramp rate, in unit of GPa and GPa/s, respectively, are sufficient. The $P_{release}$ indicates the pressure of sample decompressed close to an ambient condition. We employed a function generator and a power amplifier to tailor the input signal and a digital delay generator to operate synchronously the d-MAC/d-DAC, a CCD detector, and an oscilloscope. In Fig. 1c, different cross-sectional lattices of SWNTs correspond to the respective pressure-induced structural deformation along the load-unload pathway. In particular, we deliberately designed the pressure oscillation of cyclic ramp compression performed over the P_c - the critical collapse pressure, in order to see the influence of structural collapse on the formation of defects during long cyclic ramp loading.

TEM Characterization. High-resolution transmission electron microscopy (HRTEM) morphology was obtained by using a JEM-2100 with acceleration voltage of 200 kV and a resolution of 0.23 Å. Our TEM observations show that two SWNTs mostly aggregate into bundles and are half open-ended. The cross-sectional geometry of a bundle is, respectively, part of polygonization and circular for d_t ~1.4 and ~0.8 nm samples due to larger stiffness for smaller tubes (Fig. 1d and 1e).

Raman spectroscopy. Raman scattering excited by 2.33 eV laser (wavelength 532.5 nm) was employed to characterize the vibrational property. The spectra were recorded in a backscattering geometry by a Renishaw Raman microscope with a resolution of 1.5 cm^{-1}. The laser power tuned in a range of 10–25 mW was focused on the sample through a 50× objective. No polarization analyzer was used, so that light polarized both perpendicular and parallel to the scattering cross section was collected. To make sure a good

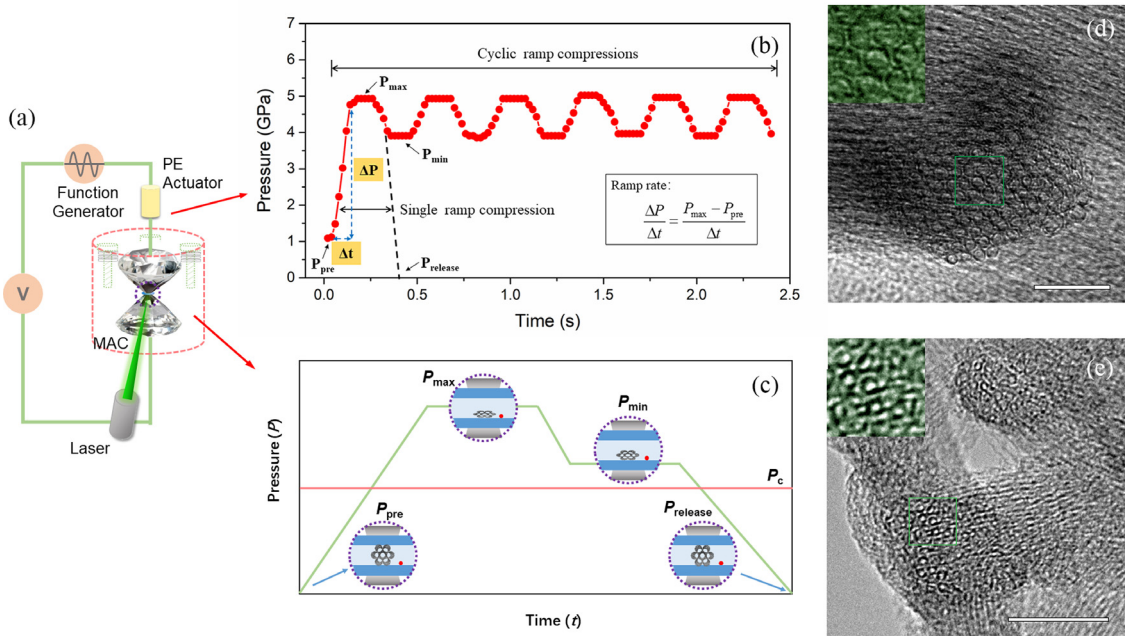

Fig. 1. (a) Schematic of the dynamic moissanite anvil cell (d-MAC) combined with time-resolved Raman spectroscopy. (b) An example of the voltage-driven trapezoidal waveforms for single and cyclic ramp compressions. The key pressure parameters include the pressure for precompression (P_{pre}), peak pressure (P_{max}), pressure oscillation ($P_{max}-P_{min}$), and pressure release ($P_{release}$). Other parameters related to time include ramp time (Δt) or ramp rate ($\Delta P/\Delta t$). (c) Four circle insets showing different cross-sectional lattices of SWNTs correspond to the respective pressure-induced structural deformation along the load-unload pathway. (d) and (e) shows the TEM image of the cross-sectional lattice of d_t ~1.4 and ~0.8 nm SWNTs, respectively. Scale bars: 10 nm.

reproducibility of data, the Raman spectra from 3 to 5 sites were randomly monitored in each test. In particular, the G-mode data obtained in the MAC was processed by carefully subtracting the low-intensity, asymmetric peak from the moissanite in the region of 1500–1550 cm^{-1}. The subtracted spectrum coincides well with those from DAC, as shown in Fig. S3.

3. Results

Phase transitions under static pressure. We first present a brief summary of phase transition identification through RBM and G modes for both samples under static pressure in two PTMs in Fig. 2 and the raw Raman spectra are given in Fig. S4. Prior static pressure experiments on SWNTs, in particular with d_t ~0.8 and ~1.4 nm as we used, have been extensively reported [20,21,35,36]. The widely used method to determine a phase transition is via the discontinuity of Raman frequency shift where a different pressure coefficient – the slope of Raman frequency as a function of pressure, occurs below and over such point. However, such discontinuity is sometimes not very obvious, instead a plateau was observed in some reports [26,29]. This plateau could be indicative of a narrow phase transition region as well. Combined with the reported results for ~0.8 and ~1.4 nm samples at similar conditions, that is, the PTM, laser wavelength, and our data, we determined those discontinuities (anomalies) as shown in Fig. 2. The criterion is either the change of pressure coefficients which values, in units of cm^{-1}/GPa, are also given on the upper of Fig. 2, or a spectral plateau. Note that the determination of those anomalies is based on the Raman data obtained in 4:1 methanol-ethanol mixture (red circles in Fig. 2a-2d). In addition, the error bars for the frequency shift and pressure are added according to the standard deviation of the Lorentzian fitting of G bands and the uncertainty of pressure determination by ruby, respectively. The RBM frequency upshifts with increasing pressure, concurrently with a drastic intensity reduction observed at ~3.7 and ~4.7 GPa for the ~1.4 and ~0.8 nm samples, respectively, though the signal quenching can

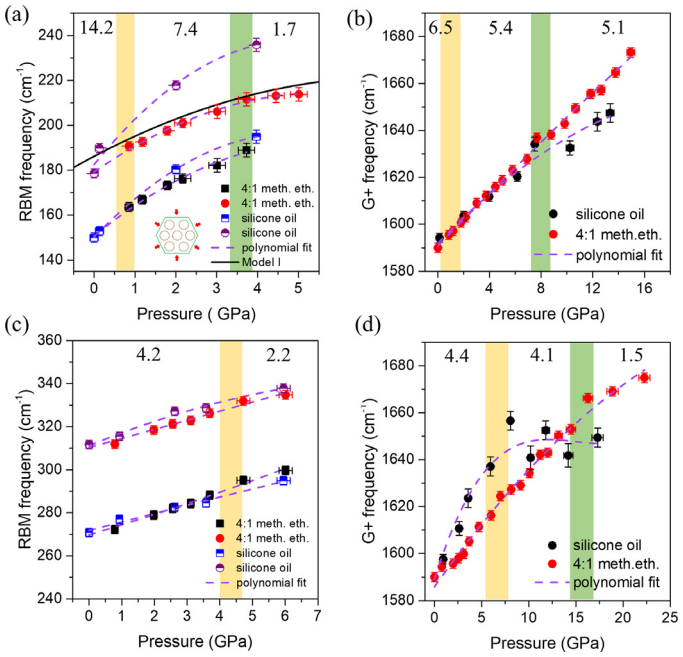

Fig. 2. Raman frequency shifts of RBM and G mode for the SWNTs under static pressure in 4:1 methanol-ethanol mixture and in silicone oil. (a, b) d_t ~1.4 and (c, d) ~0.8 nm SWNTs. The rectangles indicate narrow pressure regions of pressure-induced anomalies that are related to possible phase transitions. The values of pressure coefficients for the Raman data obtained in 4:1 methanol-ethanol mixture (red circles), in units of cm^{-1}/GPa, are also provided at the top of each panel.

be resolved up to 5–6 GPa (Fig. 2a and c), consistent with the observations by Merlen et al. [37,38]. A comparison of our data in Fig. 2a with the model I by Venkateswaran et al. may support that the bundle is subjected entirely to the external compression (see the inset of Fig. 2a) [15]. For this ~1.4 nm SWNTs, the responses

of RBM to two PTMs are considerably divergent and the pressure coefficient changes significantly with pressure increases, showing high sensitivity of these radial modes to pressure and hydrostatic environment. In contrast, the upshifts of RBM for ~0.8 nm SWNTs under pressure in two PTMs are quite similar and gentle (Fig. 2c). This stability derives from the higher stiffness of small tubes. The tangential G mode also upshifts under pressure, with a detectable intensity up to ~16 and ~22 GPa for ~1.4 and ~0.8 nm SWNTs in 4:1 methanol-ethanol mixture, respectively (Fig. 2b and d). In silicone oil, the complete quenching pressure of G mode is obviously lowered because of poor hydrostaticity. When the pressure is released, the RBM and G mode could partially recover. The reason was once considered an irreversible reduction of the translation order in the triangular lattice of a SWNT bundle, but recently new insight was proposed according to a slow recovery dynamics [20,39]. Those rectangle regions in Fig. 2 denote narrow pressure regions of pressure-induced anomalies that are related to possible phase transitions. The first anomaly for the RBM of ~1.4 nm SWNTs takes place near ~1 GPa, followed with an obvious decrease of pressure coefficient at ~3.5 GPa, which is the second anomaly. The first anomaly is usually assigned as a phase transition from circular to oval or a polygonal shape as observed by Raman spectroscopy [14,15,17,40], infrared spectroscopy [41], optical absorption spectroscopy [42], and neutron diffraction [43]. At ~5 GPa, the RBM of ~1.4 nm sample in two PTMs quenches completely. Similarly, the first anomaly of G mode of this sample is also observable at 1–2 GPa (Fig. 2b), in a good agreement with the results of RBM. Near ~8 GPa, a small plateau is shown as an indication of oval to peanut-like transition [17,44], or the symmetry loss of triangular lattice for the bundles [45]. The pressure coefficient of G mode exhibits a small decrease at higher pressures, reflecting that its structural behavior seems less influenced by pressure and the PTM. We attribute this phenomenon to the closely packed lattice and stronger intertubular interaction as evidenced by the TEM characterization (Fig. 1d), as well as by the theoretical calculation by Tersoff and Ruoff [12]. In a stark contrast, the frequency shift of G mode for ~0.8 nm sample behaves like a less compressible material above ~8 and ~16 GPa in silicone oil and in 4:1 methanol-ethanol mixture, respectively [36,37,46]. Thus the first structural transition below 10 GPa may also follow the sequence of cross-sectional transition, while the structural collapse or the formation of interlinked structures, may be responsible for the anomaly over 10 GPa [40,42].

Single ramp compression behaviors. Compared with static pressure results, the dynamic effect of hydrostatic pressure appears in all compression tests (Fig. 3). At approximate pressure, the change of G-mode lineshape and intensity becomes more prominent with the ramp rate increases. In particular, drastic intensity reduction of G mode was shown for those samples compressed in silicone oil at the most rapid rate. However, according to the direct observation of D mode, no obvious change of I_D/I_G ratio which is related to deformation-induced structural defect or lattice disorder was observed in silicone oil under all dynamic conditions as shown in Fig. S5. Note that there exists a certain amount of pre-existing defects according to a clear profile of D mode with the I_D/I_G of ~0.046. By the most rapid compression (~7700 GPa/s), the I_D/I_G of ~0.8 nm SWNTs goes to 0.075 and the G mode quenches at nearly ~8.8 GPa (Fig. 3e), also far below the static result of ~22 GPa. The static and dynamic compression results of RBM for ~0.8 nm sample are also given in Fig. S6, while the RBM profiles for ~1.4 nm sample is not available since the overlap of a strong peak at 149.6 cm^{-1} from the moissanite and our samples (~142–185 cm^{-1}). The Raman profiles of G mode of both samples before and released from those compressions under other dynamic conditions (medium- and low-rate) are compared in Fig. S7. The recovery hysteresis for both samples tend to be more remarkable

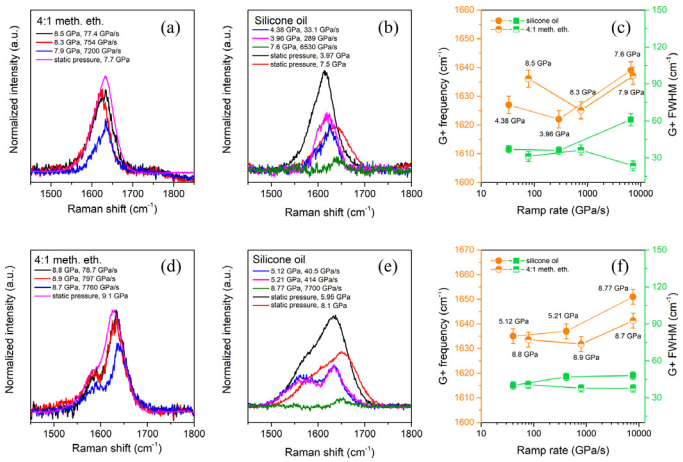

Fig. 3. Comparison of the G-mode profiles, the G^+ frequency shift and the FWHM of SWNTs under static and single ramp compressions with different ramp rates in 4:1 methanol-ethanol mixture and in silicone oil. (a, b, c) d_t ~1.4 and (d, e, f) ~0.8 nm SWNTs.

when the ramp rate becomes faster. Lebedkin et al. reported the pressure-induced irreversible damage of d_t ~0.7 and ~1.4 nm debundled nanotubes occurs below the dramatic cross-sectional distortion (collapse) [47]. They found that the I_D/I_G ratio goes as high as 0.42 from 0.09 for the pristine sample after a compression up to 8 GPa for 10 min and they attributed this to the formation of massive kinks in structure. However, no obvious irreversible structural transition was observed below 13 GPa, but some permanent damage could be further induced by a high pressure in a wide range of ~20–30 GPa by the results of Yao et al. [19,21,40]. Yao et al. found that two starting SWNTs with the I_D/I_G ratio of 0.06 and 0.007 showed a different capability of resilience after a decompression from a high pressure of 30 and 16 GPa (I_D/I_G ~0.87 and 0.13), respectively. A recent study by Shen et al. investigated carefully the contribution of different types of defects to the pressure-enhanced D mode, and discussed the recovery dynamics [20]. Their results showed that the intensity and lineshape of D mode was totally changed by a pressure of 4 GPa, though all components return within small margins to original ones. The I_D/I_G ratio changes from 0.19 (ambient) to 0.47 (4 GPa). In contrast, we do not observe a pressure-induced multi-peaked asymmetry of D mode in this work, thereby we interpret that the difference of our results derives from the sample configuration they used. In fact, another work of shock wave compression behavior of double-walled carbon nanotubes by Mases et al. may support our results. The authors found minor damage can be detected below a threshold of 19–26 GPa under shock compression [48].

To survey the dependence of Raman scattering of SWNTs on ramp rate, the frequency shift and the full width at half maximum (FWHM) of the most intense G subpeak (G^+) as a function of ramp rate are plotted in Fig. 3c and f. The responses of two SWNTs to peak pressure, ramp rate and PTM are different. For ~1.4 nm SWNTs, the G^+ frequency shift demonstrates a more significant influence by peak pressure, rather than ramp rate. On the other hand, the broadening of G^+ subpeak seems more obvious in silicone oil, leading to a larger change of FWHM of ~30 cm^{-1}. For ~0.8 nm SWNTs, the influence of silicone oil is more prominent even at low pressure near 5 GPa. In 4:1 methanol-ethanol mixture with a better hydrostaticity, the effect of dynamic loading can be also seen via a frequency upshift of ~10 cm^{-1} for the cases at low- to high-rate compressions. In contrast to larger tubes, the FWHM of ~0.8 nm sample shows a very small change of ~4 cm^{-1} from low- to high-rate compression.

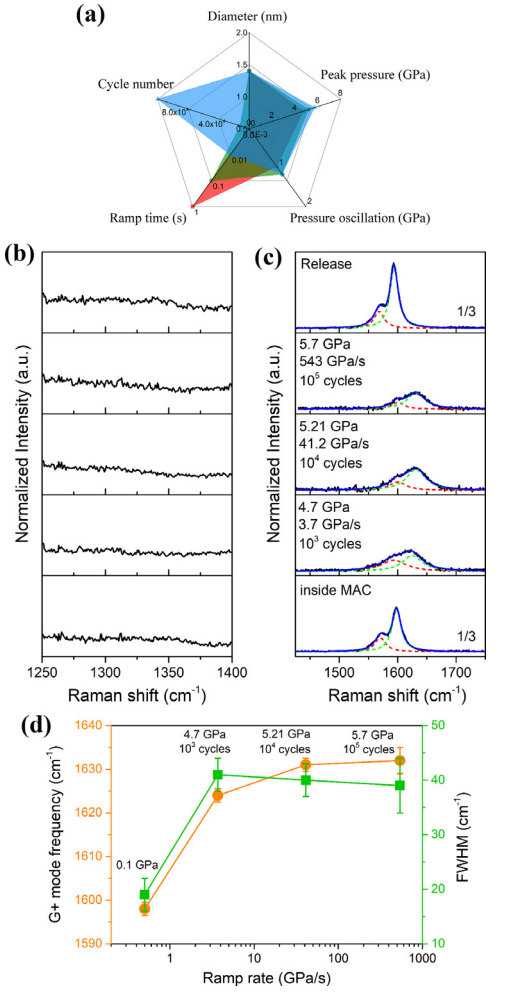

Fig. 4. Cyclic ramp compression behaviors of SWNTs with d_t ~1.4 nm in silicone oil. (a) The experimental variables of cyclic ramp compression include peak pressure, pressure oscillation, ramp time and cycle number. (b) Raman D and (c) G modes of the sample under different conditions as indicated. (d) shows the G^+ mode frequency shift and the FWHM versus ramp rate.

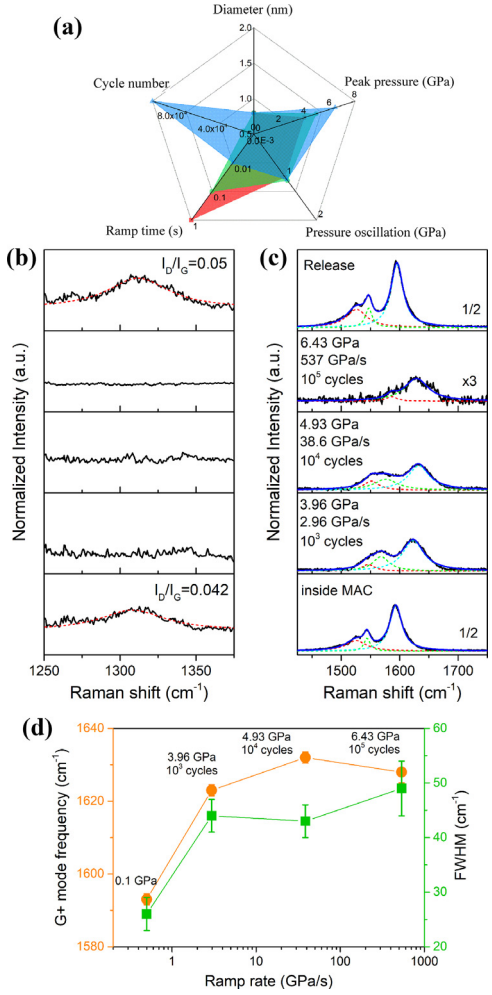

Fig. 5. Cyclic ramp compression behaviors of SWNTs with d_t ~0.8 nm in silicone oil. (a) The experimental variables of cyclic tests for this sample. (b) Raman D and (c) G modes of the sample under different conditions as indicated. (d) shows the G^+ mode frequency shift and the FWHM versus ramp rate.

Cyclic ramp compression behaviors Fig. 4a exhibits the experimental variables of cyclic ramp compression for ~1.4 nm sample, including peak pressure (P_{max}), pressure oscillation ($P_{max}-P_{min}$), ramp time (Δt) and cycle number (N). All cyclic tests were intended to be performed in silicone oil to avoid pressure release due to the easy volatilization of alcohols. The most extreme condition is given as follows: P_{max} ~5.7 GPa, $P_{max}-P_{min}$ ~1.2 GPa, Δt ~10 ms, and N ~10^5 cycles. As shown in Fig. 4b and c, the D and G modes of ~1.4 nm sample under different cyclic conditions are compared. No obvious change of D mode was found in all test conditions, showing high structural stability. The lineshape of G mode reveals a slow broadening as pressure and ramp rate increases. By the change of the frequency shift and the FWHM in Fig. 4d, we found this ~1.4 nm sample is rather stable to pressure, ramp rate and cycle number. Fig. 5a exhibits the experimental variables of cyclic ramp compression for ~0.8 nm sample as well. The most extreme condition is listed as follows: P_{max} ~6.4 GPa, $P_{max}-P_{min}$ ~1.0 GPa, Δt ~10 ms, and N ~10^5 cycles. In Fig. 5b, there is a very small increase of I_D/I_G ratio after above cyclic compression which is indicative of very few pressure-induced defects. Furthermore, the recovered Raman lineshape matches well with that of the starting sample, though a spectral broadening occurs during compression as well. In addition, the cyclic behavior of RBM for ~0.8 nm sample also shows a full recovery as shown in Fig. S6. In subsequent tests, we failed to raise pressure and ramp rate since the MAC was broken by the abrasive scratches formed on the culet's surface during cyclic compression. In other words, the experimental limit allowed for cyclic experiments is far below the strength limit of moissanite anvils capable of a static pressure over 50 GPa [49]. Generally, our results demonstrate a faster recovery process of SWNTs under dynamic compression. In a stark contrast, the increase of D intensity upon static deformation recovers slowly to ambient condition [20]. The average I_D/I_G ratio for the ~1.4 and ~0.8 nm SWNTs after 10^5 cyclic compressions is 0.024 and 0.05, respectively, compared with 0.009 and 0.042 measured from the pristine samples. Different from the single ramp compression, no obvious loss of G-mode intensity was observed in Fig. 4 and Fig. 5. We account for the lower peak pressure applied in those cyclic tests. Other G-mode profiles of the samples before and after cyclic ramp compression (N ~10^4 and 10^3 cycles) are also compared in Fig. S8. An unusual phenomenon that a larger G-mode intensity of the recovered sample relative to the starting sample for ~0.8 nm SWNTs was even observed and the reason needs further clarification. Shen and Zerulla recently performed repeated static compression (3 cycles) on the same ~0.8 nm SWNTs as we used. They found that SWNTs was fully reversible to 4 GPa but within a long recovery time ~100 min [20]. Our results provide new evidences

that the SWNTs subjected to dynamic and cyclic loading possess faster recovery capability and ultrahigh structural stability.

4. Discussion

The role of PTM under dynamic pressure. The issue of PTM effect on structural behaviors of CNTs has been widely studied in terms of either surface adsorption or internal filling of PTM molecules. The Raman evidence by Amer et al. supported an adsorption mechanism, rather than a collapse mechanism, to explain the extended spectral plateaus of tangential G mode observed [50]. Different from Amer et al., Proctor et al. found that the penetration of PTM molecules into the interstitial spaces between nanotubes in a bundle plays a key role in the nanotube's response to applied hydrostatic pressure, and some solvents, e.g., hexane and butanol, could not absorb onto the nanotube surface at low pressures [51–53]. The experimental results by Merlen et al., however, suggested that a negligible effect of PTM on RBM, but the tangential G mode is strongly affected by the PTM. Furthermore, their results supported a picture that the alcohol molecules should not enter the tubes [37]. Honda et al.'s result was nearly opposite to that by Merlen et al. They concluded that, an increase of RBM frequency shift with the molecular weight of the solvents – the so-called choking effect, while the G mode is insensitive to solvent adsorption [54]. But the dependence of G mode transition upon molecular weight of solvents was reported by Gao et al. [55]. Using analytical methods and molecular dynamics simulation, the surface absorption mechanism of PTM molecules for RBM upshift under pressure was verified by Longhurst et al. [56]. According to the work by Abouelsayed et al., the infrared absorbance spectra of SWNTs under pressure exhibits a pressure-induced shift for all cases of PTM employed [57]. The role of PTM only affects the critical pressure P_c quantitatively. The authors thought that the intercalation or adsorption of argon and helium could prevent the deformation of the tubes, thus they expected the absence of an anomaly. Nevertheless, an anomaly was observed in all cases, and they questioned the proposed importance of PTM regarding the occurrence of the structural transition. Yao et al. found that the intercalation or adsorption of the PTM, like argon, could prevent the deformation of the tubes and thus affect the reversibility of the SWNTs decompressed from high pressures [21]. The comparison of high-pressure experiments with and without methanol-ethanol mixture in their previous work also supports this conclusion [19]. The recent work by Bousige et al. gives new insight on understanding the molecule filling in CNTs [35]. The authors provide a new spectroscopic signature to determine the onset pressure of collapse – the pressure at which G mode softens while RBM vanishes. According to prior studies as mentioned above, the filling effect of PTM can be extracted from the relative changes of continuous spectral shift in comparative static pressure tests with different PTMs. But the data collection of dynamic experiment will invalidate this method since the dynamic data only includes a starting and a final point. So, we could take another way to estimate the filling of PTM molecules, that is, the structural reversibility of deformed nanotubes. As mentioned above, molecule filling could lead not only to an enhancement of collapse pressure, but also to a higher structural reversibility when the pressure is unloaded. As shown in Fig. S7, the complete reversibility of single-ramp-compressed nanotubes deteriorates when the ramp rate become higher. This evidence implies that dynamic compression with a ramp time less than 100 ms is too short to make a complete diffusion of PTM molecules into the internal space of nanotubes. Therefore, the pressure-induced deformation in the empty region of nanotubes may be severe. This tentative conclusion can rationally explain the reason for the remarkable reduction of G mode intensity as well. In this sense, it is reasonable to speculate that cyclic dynamic loading may be favorable for the continuous insertion of liquid molecules, thus resulting in higher structural reversibility. The Raman results for ~1.4 nm sample in Fig. 4, S8a, S8b agree well with the speculation. With cyclic number increases up to 10^5, the Raman profiles of G mode of decompressed ~1.4 nm sample can almost recover to the original one. Different from ~1.4 nm SWNTs, all cyclic compressed samples with d_t ~0.8 nm show a full reversibility regardless of loading conditions (Fig. 5, S8c, S8d). This result may suggest that the molecule insertion to ~0.8 nm nanotubes can rapidly achieve by cyclic loading due to a short length and weak bundling of small nanotubes. To verify clearly this issue of PTM's role in dynamic loading, theoretical calculations and simulations are further required.

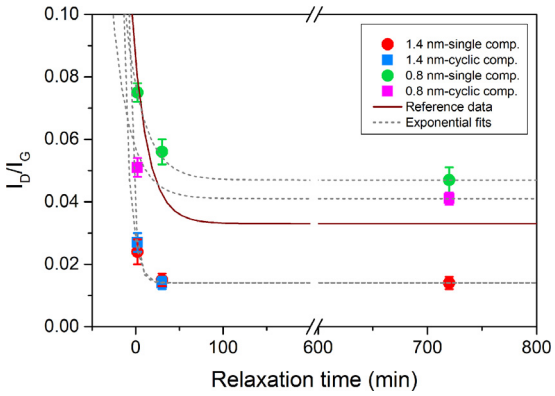

Fig. 6. Recovery dynamics of the SWNTs under single and cyclic ramp compressions determined by the I_D/I_G ratio versus relaxation time. All cases presented are the results obtained under the most extreme condition of each group in silicone oil. The reference data is reproduced from the static pressure results for ~0.8 nm SWNTs by Shen and Zerulla.

Recovery dynamics and energy dissipation. Upon static deformation, the pressure-induced defects or lattice disorder of SWNTs has drawn substantial concerns [19-21,40]. Recently, a time-dependent recovery mechanism for pressure-induced D mode was proposed by introducing a mono-exponential, Arrhenius-type function [20]. Here, the time-dependent behaviors of I_D/I_G ratio versus relaxation time for our samples under the most extreme condition in single and cyclic ramp tests are plotted in Fig. 6. Other recovery results at different conditions are additionally given in Fig. S9. We found that all samples could achieve more than ~90% recovery within 30 min. The highest ramp rate in single ramp compression seems more influential on smaller tubes according to a larger increase of $\Delta I_D/I_G$, specifically, $\Delta I_D/I_G$ ~0.015 and ~0.029 for ~1.4 and ~0.8 nm SWNTs, respectively. Below this extreme rate, their recovery behaviors are quite similar. When the pressure is released, the ~1.4 nm SWNTs would recover faster than ~0.8 nm sample, implying a smaller elastic hysteresis. This is inconsistent with previous understanding that smaller tubes are usually stiffer due to larger curvature effect, therefore their load resistance and recovery rate is better than larger tubes [58]. We ascribe this phenomenon to the higher structural stability induced by highly close-packed lattice (polygonization) of ~1.4 nm SWNTs as revealed by Fig. 1d. This polygonal section was predicted a metastable state by first-principles calculations, which is too rigid to reduce tube volumes and intertubular vdW repulsion [59]. To quantify this bundling effect, a packing factor was proposed and yields a decrease of axial property. For (10, 10) SWNT ropes (d_t ~1.35 nm), the packing factor is theoretically estimated to be ~1.7 [60]. This enhancement by bundling, in fact, results from $\sigma^*-\pi^*$ hybridization induced by the faceting [61]. Upon cyclic ramp compressions (Fig. S9), the approximate result of I_D/I_G ratio shows a less dependency of pressure-induced deformation in SWNTs upon current cycle number (10^3–10^5) and ramp rate (3–540 GPa/s). However, the

recovery dynamics varies with nanotube diameter. In Fig. 6 and S9, the exponential fits to the I_D/I_G ratio under respective dynamic conditions are carried out by $I_D/I_G(t) = c + a\exp(-t/\tau)$, where τ is the mean recovery lifetime, c the baseline and a an scaling parameter [20]. From high- to low-rate compression in single ramp compression tests, the change of τ value follows a sequence of, in unit of min, 8→5→4 and 21→18→9, for ~1.4 and ~0.8 nm SWNTs, respectively. This means that the recovery rate of ~1.4 nm sample is about 2–3 times faster than that of ~0.8 nm sample, also demonstrating the role of lattice polygonization on mechanical stability. We also reproduced the reference data of I_D/I_G evolution for ~0.8 nm SWNTs upon static compression (~4 GPa) for comparison (solid line in Fig. 6) [20]. Taking experimental discrepancies into consideration, the τ value of our result obtained at similar pressure of ~5 GPa, i.e., τ value in the range of 9–18 min, is reasonable in comparison with the reference result (~17 min). Also, the inflection point of the fitted curve can be regarded as the end of elastic recovery, or, the stable stage of the SWNTs. We found that all inflection points of dynamic compression data are prior to that of static pressure result, showing a faster recovery behavior [28].

The issues on the energy storage and dissipation of SWNTs under strain are of fundamental and engineering importance. Chesnokov et al. measured quantitatively the energy storage of SWNTs during a large and reversible volume reduction [1]. They found that the reversible work of their sample in compression to ~2.9 GPa was determined to be ~0.18 eV/atom. Pathak et al. reported higher recovery of SWNTs to axial elastic deformation at faster strain rates results from better energy dissipation mechanism [28]. However, it is unfortunate that the energy storage and dissipation of SWNTs under dynamic radial compression has not been reported to our knowledge. From the theory of solid mechanics, the volume deformation specific energy can be expressed by a combination of volume and shape change specific energy. The pressure-induced volume deformation specific energy therefore can be calculated as a measure of stored elastic energy in whole SWNTs. For hydrostatic pressure, the term of shape change specific energy is neglected, and we could obtain the volume deformation specific energy by a formula of $v_\varepsilon = \frac{1}{2}\frac{\Delta V}{V_0}p$(see more details in Section 1 and Fig. S12 in SI). Then, to characterize the material damping response to stored elastic energy, a dimensionless loss coefficient, η, which measures the fractional energy dissipated in a load-unload cycle needs further calculation [62]. The calculation method is presented in Section 2 in SI. Two key physical quantities, the stored energy U and the dissipated energy ΔU, correspond to different integrated areas in the curve of pressure as a function of volume variation, $\Delta V/V_0$ (Fig. S13). In addition, the mode Grüneisen equation is also required to link volume ratio (V/V_0) with phonon frequency shift (ω/ω_0) to satisfy our scenario. In a crystal, strain arises when it is deformed, and in turn, modifies the phonons. Tensile strain usually results in mode softening while the opposite for compressive strain. The mode Grüneisen parameter, γ, is proportional to the magnitude of frequency shift of phonons [63]. Different from the 2D and 3D graphitic structures (see Fig. S10), the pressure-induced frequency shift of Raman mode is related to the compression of 1D structure by mode Grüneisen parameter, which is commonly derived from [64,65]:

$$\omega(P)/\omega_0 = [V(P)/V_0]^{-\gamma} \quad (1)$$

For G phonon, this Grüneisen scaling relation yields γ_G which strongly vary with mode frequency [66]:

$$\gamma_G = -\frac{V}{\omega_G}\frac{d\omega_G}{dV} = -\frac{d\ln\omega_G}{d\ln V} = \frac{1}{\kappa}\frac{d\ln\omega_G}{dP} = B_0\frac{d\ln\omega_G}{dP} \quad (2)$$

where ω_G is the G mode frequency, V the crystal volume, P the pressure, κ the compressibility, and B_0 the isothermal bulk modulus at zero pressure. Like layered graphite, the highly anisotropic configuration usually leads to high-energy vibrations, in this case, G^+ phonon, with $\gamma_G << 1$. A least-squares fit to the relation $\omega(P)/\omega_0 = [(\delta_0/\delta')P + 1]\delta'$, where δ_0 and δ' is the logarithmic pressure derivative $(d\ln\omega/dP)_{P=0}$ and the pressure derivative of $d\ln\omega/dP$, respectively, is commonly used to calculate γ_G ($B_0\delta_0$) [65]. Our data fits for ~1.4 and ~0.8 nm SWNTs under static pressure are shown in Fig. S11. The δ_0 and δ' values are about 0.0033 (0.0026) and 0.33 (0.41) for ~1.4 (~0.8) nm samples. For ~1.4 nm SWNTs, the experimental result of B_0 is in a wide range of 13–43 GPa, compared with ~34 GPa for graphite [45,61,65,67]. By taking the compressibility of 0.024 GPa^{-1}, we obtained the γ_G ~0.138 for ~1.4 nm SWNTs, close to the result by Sood et al. [18]. It should be pointed out that the bulk modulus B_0 is also diameter-dependent with a saddle-shaped or monotonic distribution by elasticity calculations [12,68,69]. We employ the B_0 of 37 GPa calculated for (6,6), (10,0), (8,4) SWNTs, which have similar diameters (0.78–0.82 nm) to our smaller sample with ~0.8 nm [70]. Thus the γ_G for ~0.8 nm SWNTs is reasonably estimated to be ~0.096. Following above procedures, we summarize the results about the stored elastic energy and energy dissipation of our samples under static and dynamic pressure in two PTMs as shown in Fig. 7. The stored elastic specific energy of two SWNTs that statically compressed to the complete G-mode quenching in 4:1 methanol-ethanol mixture and in silicone oil is compared in Fig. 7a. Such a value can also be considered a maximum capability of energy storage of SWNTs for each condition. The result demonstrates that the silicone oil is probably not favorable to store deformation energy due to its poor hydrostaticity. In 4:1 methanol-ethanol mixture with good hydrostaticity, the ~0.8 nm SWNTs stores near two times larger elastic specific energy than that of ~1.4 nm SWNTs. This is consistent with a fact that smaller tubes usually have a larger volume deformation and higher G phonon quenching pressure. From the classic Lévy-Carrier law, the ~0.8 nm SWNTs collapse at a three times higher pressure compared with the pressure for ~1.4 nm SWNTs [9]. This applies as well to the case of complete phonon quenching. For example, according to our static pressure results, the G mode of ~1.4 and ~0.8 nm SWNTs fully quenches at 14.9 and 22.3 GPa, resulting in a $\Delta V/V_0$ of ~0.29 and ~0.43, respectively. This is probably the reason for the larger energy storage capability for ~0.8 nm sample. As simulated by Bousige et al., the value of $\Delta V/V_0$ for individual and bundled (6, 5) SWNTs (d_t ~0.8 nm) after the complete collapse could achieve ~0.45 at ~24 GPa, and ~0.35 at ~16 GPa, respectively [35]. Due to a fact that a number of ~0.8 nm SWNTs are individual or weakly bundled as shown in Fig. 1e, our result agrees well with the result by Bousige et al. Fig. 7b shows the corresponding loss coefficient of two SWNTs in 4:1 methanol-ethanol mixture. The loss coefficients in a narrow range of 0.014 to 0.016 may denote a similar energy dissipation behavior for two SWNTs upon static decompression. However, the scenario for those SWNTs under single ramp compression seems more complex. Under identical conditions, all results of ~0.8 nm sample display higher energy storage capability at the ramp rate from an order of magnitude of 10 to 10^3 GPa/s (Fig. 7c). With the increase of ramp rate, the stored energy of smaller tubes also increases more significant than that of larger tubes at similar peak pressure, for example, the data in the pressure range of 8–9 GPa. Fig. 7d shows the corresponding loss coefficient of two SWNTs under single ramp compression. Generally, the data reveals a higher energy dissipation for ~0.8 nm sample by the distribution of loss coefficient falling within 7–9 GPa (η ~0.005–0.025), compared with the η ~0.002–0.017 for ~1.4 nm sample. Those abnormal data in 5–6 GPa for ~1.4 nm sample in silicone oil is as high as ~0.04. Though the reason is still unclear, the intertubular vdW interaction and the polygonal lattice may be at play. We assume that a small deformation may be dissipated faster than a large one due to strong repulsion to strain in polyg-

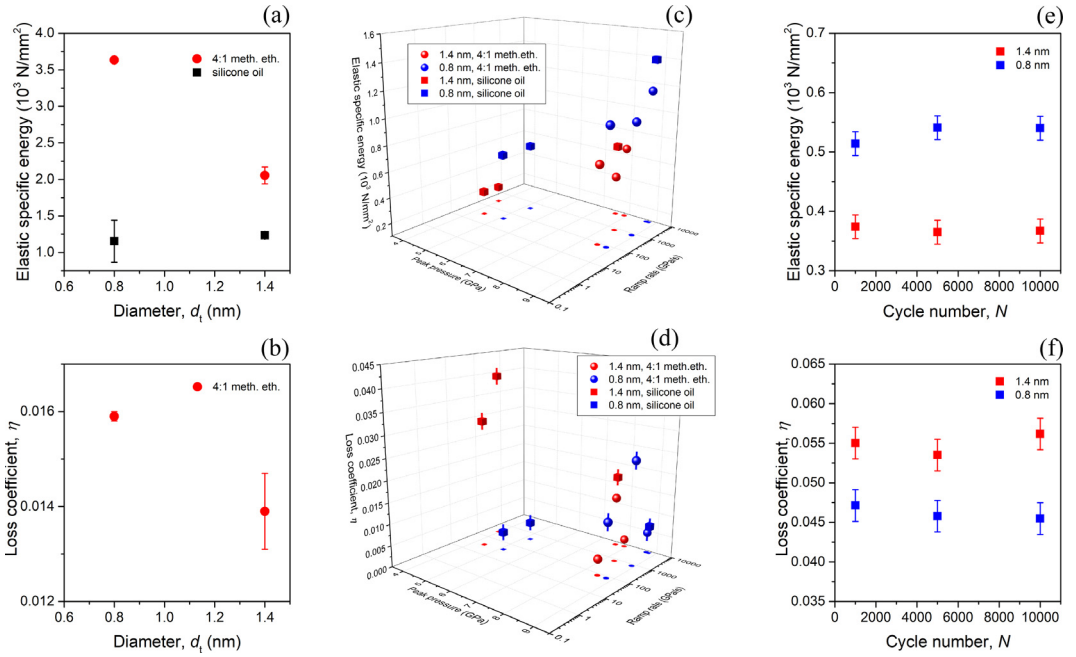

Fig. 7. Elastic energy storage and dissipation of SWNTs under (a, b) static, (c, d) single and (e, f) cyclic ramp compressions in 4:1 methanol-ethanol mixture and in silicone oil. In particular, (c, d) shows the stored elastic energy and loss coefficient as a function of ramp rate and peak pressure, respectively. (e, f) shows the energy storage and dissipation of the SWNTs at selected intermediate events during a cyclic ramp compression test with N$\sim 10^4$.

onal lattice. To monitor the energy storage and dissipation behavior of SWNTs during cyclic ramp compression, the elastic specific energy and loss coefficient at a selected intermediate cycle with i = 1000, 5000, 10,000 cycle are compared in Fig. 7e and f. The corresponding calculation method is given in Section 3 in SI. Our results display a very small fluctuation of either the elastic specific energy or the loss coefficient for two SWNTs during cyclic ramp compressions, showing a desirable feature of steady energy conversion at the molecular level.

Phase transitions under dynamic pressure. In theoretical studies, the discontinuities of some physical quantities, such as lattice constant (a), volume reduction (V/V_0), thermodynamic quantities (e.g., enthalpy) and system energy variation (ΔE) of SWNTs, are usually employed to explain the spectroscopic anomaly in experimental measurements under static pressure [9,10,14,59,71]. One of the most key discontinuities of phase transition of SWNTs under global radial deformation is depicted by the critical pressure P_c – the pressure of RBM quenching or the first anomaly of G mode for Raman spectrum. In contrast, the pressure of G-mode quenching, i.e., the complete suppression of high-energy A, E_1, and E_2 vibrations, is usually several times larger than the P_c determined by G mode.

In this work, however, we observed an interesting phenomenon that the quenching pressure of G mode under dynamic pressure drops significantly even to the onset of 'normal' phase transition region under static pressure, as shown in Fig. 8. The hatched and solid area indicates the 'normal' phonon-mode transition region under static compression in 4:1 methanol-ethanol mixture and in silicone oil measured in this work, respectively. The circles denote the collapse pressure or the critical point of structural transition under various static pressure conditions in the literature dataset built by data mining method. The squares and triangles indicate the respective phonon quenching pressure of G-mode and RBM under the most rapid compression in silicone oil. It should be pointed out that such result in 4:1 methanol-ethanol mixture is still inconclusive by current experimental results. Due to good hydrostaticity, the pressure of complete G-mode quenching in 4:1 methanol-

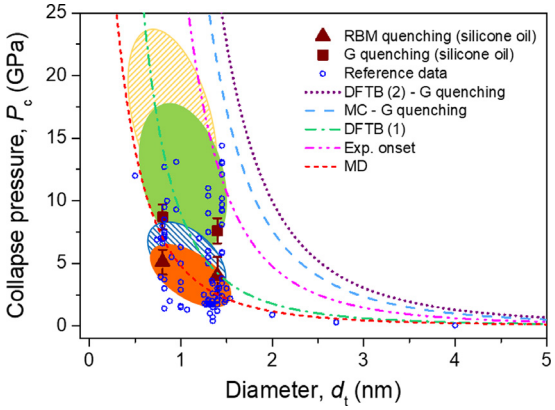

Fig. 8. The experimental (circles) and theoretical (dash lines) results of tube collapse pressure P_c versus diameter d_t for static compression in literature. For comparison, the oval regions determined by our results show the onset and complete of phase transition for the RBM (small ovals) and G mode (large ovals) of SWNTs under static pressure in 4:1 methanol-ethanol mixture (hatched area) and in silicone oil (solid area). In addition, the quenching pressure of the RBM and G mode under the most rapid compression is also plotted.

ethanol mixture is much higher than in silicone oil. So far, the concurrent combination of high ramp rate and higher pressure is a challenge for our device. The predicted lines of P_c by MD and DFTB basically agree with our data and published results. Moreover, the predictions on G mode quenching by DFTB and MC methods show the corresponding pressure of phonon suppression is far greater than P_c. Thus, past experimental and theoretical results obtained from static pressure would fail to explain our data. On the other hand, we are very interested in what happened to SWNTs under dynamic compression and how to characterize quantitatively the deformation-induced difference of samples between static and dynamic hydrostatic pressure by Raman results. So let's make a closer look by theory, the RBM derives from the out-of-plane vibration along the tube's radii, whereas the G^- and G^+ results from

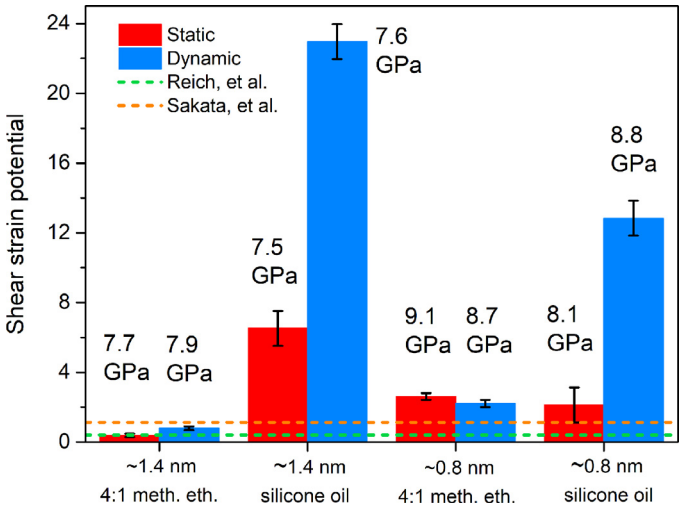

Fig. 9. Comparison of the shear strain potentials of SWNTs under static and the most rapid compression at a close peak pressure as indicated. The details are also available in Figs. S14, S15, and Table S1 in SI. Two dash lines are the results from the literature by Reich et al. and Sakata et al.

in-plane vibrations along the circumferential and axial directions, respectively [72]. The responses of these phonon modes to hydrostatic strain are different. Since SWNTs is anisotropic, the strain tensor from hydrostatic pressure can be described by two fully symmetric strain components, $\varepsilon_{\theta\theta}$ along the circumference and ε_{zz} along the axis, derived by the theory of line groups for 1D system [73,74]. According to the line group theory and dynamic equation for phonon mode in the presence of strain, the shear strain in SWNTs under hydrostatic pressure can be obtained by the method by Reich, et al. [75]. The detailed information on how to calculate the shear strain potential of SWNTs is given in Section 4 in SI. The most key equation is presented as follows:

$$\frac{\Delta\omega}{\omega_0} = \frac{\left(\tilde{K}_{11}+\tilde{K}_{12}\right)}{4\omega_0^2}\left(\varepsilon_{\theta\theta}+\varepsilon_{zz}\right) \pm \frac{1}{2}\frac{\left(\tilde{K}_{11}-\tilde{K}_{12}\right)}{2\omega_0^2}\left(\varepsilon_{\theta\theta}-\varepsilon_{zz}\right) \qquad (3)$$

where the $\tilde{K}$ is the symmetric tensor in the dynamic equation for phonon modes in the presence of strain [76], ω_0 the strain-free frequency. The first term $(\tilde{K}_{11}+\tilde{K}_{12})/4\omega_0^2$ and the second term $(\tilde{K}_{11}-\tilde{K}_{12})/2\omega_0^2$ is the deformation potential under hydrostatic and shear strains, respectively. In Fig. 9, we summarize the calculated shear strain potential of SWNTs under static and the most rapid compression in two PTMs. For comparison, we also add the shear strain of SWNTs under static pressure by Reich, et al., as well as of graphite fibers under uniaxial stress by Sakata, et al. [75,77]. Our result is a clear manifestation of the presence of shear strain induced by the dynamic loading in different PTMs. In particular, the synergistic effect of dynamic load and PTM leads to a remarkable increase of shear strain potential in SWNTs as shown in the cases in silicone oil. Apart from the case of ~0.8 nm sample in 4:1 methanol-ethanol mixture, the shear strain potential in other cases under dynamic load is generally greater than that under static compression. The different result for ~0.8 nm sample in 4:1 methanol-ethanol mixture may be relevant to the higher stiffness of smaller tubes, as well as the weakly bundled configuration. Furthermore, we should give a glance at the recent work by Chen, et al. that reported the differences between 4:1 methanol-ethanol mixture and silicone oil under pressure [78]. According to their experiments, there is a small deviation stress (σ/P <0.1) near 5 GPa for silicone oil. Besides, the hydrostaticity of silicone oil could maintain up to 10 GPa. What's more, the authors also found that Raman spectroscopy seems to be less sensitive than synchrotron x-ray diffraction in catching subtle transitions related to hydrostaticity variations in the two PTMs. For our cases in 4:1 methanol-ethanol mixture, the shear effect exists in both samples, though the enhancement of such effect induced by dynamic load seems very limited. The value for the ~1.4 nm sample is consistent to the results for the SWNTs with a similar diameter by Reich et al. [75]. As shown in Fig. 3d, the Raman spectra of G-mode for the ~0.8 nm sample in these two PTMs display an obvious change in intensity, rather than frequency shift. This may explain a similar shear strain potential for the case of ~0.8 nm sample in 4:1 methanol-ethanol mixture since the theoretical analysis is only carried out based on frequency shift. No other factor is considered, such as the lineshape symmetry and intensity. Karmakar et al. also reported similar phenomenon that the G-mode quenching of d_t ~1.5 nm SWNTs under non-hydrostatic pressure occurs at much lower pressures than that under hydrostatic pressures [39]. Their Raman profiles of G modes are only discernable up to 7 GPa, in a good agreement with our result for ~1.4 nm sample. However, they explained the reason in a simple way that non-hydrostatic pressure yields a much high degree of deformation. Another neutron diffraction result by Rols et al. on ~1.3 nm SWNTs under non-hydrostatic compression also indicated the final polygonization could finish at ~5 GPa [43]. Actually, the shear strain component induced by dynamic load is common. Similar effect of high percentage of shear force in hydrostatic pressure on the reduction of the critical pressure of phase transitions was also observed in same group elements, Si and Ge crystals [79,80].

5. Conclusions

In this work, we present a detailed investigation on the dynamic effect of hydrostatic pressure on the structural and vibrational properties of two SWNTs with d_t ~1.4 and ~0.8 nm in 4:1 methanol-ethanol mixture and in silicone oil. Some conclusions can be drawn as follows: (1) a common phenomenon is found that the lineshape and intensity of G mode of SWNTs is influenced by dynamic load to varying degrees in two PTMs, indicating the universality of dynamic effect of hydrostatic pressure. In particular, this effect is largely enhanced in silicone oil. For example, with the ramp rate increases to an order of magnitude of 10^3 GPa/s, the critical pressure of complete G-mode quenching for both samples are remarkably lowered compared with results from static pressure. (2) In silicone oil, no obvious pressure-induced defects or lattice disorders is usually observed for both SWNTs upon cyclic ramp compression (10^3–10^5 cycles) with varying ramp rates, showing excellent cyclic structural stability and good resilience under extreme dynamic conditions. (3) The elastic recovery behaviors of both samples under dynamic pressure can be well described by the exponential fitting. The similar recovery behaviors for ~1.4 nm SWNTs under single and cyclic compression may result from the lattice polygonization which provides additional resistance by vdW interaction to strain. (4) According to the calculation of elastic specific energy and loss coefficient of SWNTs under ramp compression, the ~0.8 nm sample shows a higher capability of elastic energy storage, but its dissipation behaves similar to that of ~1.4 nm sample under identical conditions. For selected intermediate cycles, the elastic specific energy and loss coefficient of SWNTs under cyclic ramp compression display an approximate degree, which further demonstrate that SWNTs has a stable property of work-energy conversion and energy storage-release at the molecular level. (5) The shear strain potential induced by either dynamic pressure or the PTM is theoretically analyzed by the frequency shift of G mode. Our results imply that the shear strain potential in SWNTs could be largely enhanced by the combination effect of dynamic pressure and the hydrostaticity deterioration of PTM.

The dynamic loading device presented opens up opportunities in the study of novel metastable phases and physical transforma-

tions of low-dimensional materials [34]. The electrical and other fundamental properties of SWNTs under dynamic loading, which are significant for fundamental science and applications, need further investigations.

Declaration of Competing Interest

All authors declare that NO conflict of interest exists.

Acknowledgements

The authors acknowledge the financial support of the National Natural Science Foundation of China (No. 51871180 and 21627802), the Strategic Priority Research Program of Chinese Academy of Sciences (No. XDB17000000), and the National Key R&D Program of China (No. 2021YFB3701203). B. Li and X. Zhang are also supported by the Doctoral Teacher Starting Fund of Xi'an University of Technology (No. 101–451121007 and 101–451121008).

Supplementary materials

Supplementary material associated with this article can be found, in the online version, at doi:10.1016/j.actamat.2022.117776.

References

[1] S.A. Chesnokov, V.A. Nalimova, A. Rinzler, R.E. Smalley, J.E. Fischer, Mechanical energy storage in carbon nanotube springs, Phys. Rev. Lett. 82 (1999) 343.
[[2] M.J. Lopez, A. Rubio, J.A. Alonso, L.C. Qin, S. Iijima, Novel polygonized single-wall carbon nanotube bundles, Phys. Rev. Lett. 86 (2001) 3056.
[3] J. Zang, A. Treibergs, Y. Han, F. Liu, Geometric constant defining shape transitions of carbon nanotubes under pressure, Phys. Rev. Lett. 92 (2004) 105501.
[4] L. Vitali, M. Burghard, P. Wahl, M.A. Schneider, K. Kern, Local pressure-induced metallization of a semiconducting carbon nanotube in a crossed junction, Phys. Rev. Lett. 96 (2006) 086804.
[5] A. Barboza, A.P. Gomes, B.S. Archanjo, P.T. Araujo, A. Jorio, A.S. Ferlauto, M. Mazzoni, H. Chacham, B.R. Neves, Deformation induced semiconductor-metal transition in single wall carbon nanotubes probed by electric force microscopy, Phys. Rev. Lett. 100 (2008) 256804.
[6] M. Huang, Y. Wu, B. Chandra, H. Yan, Y. Shan, T.F. Heinz, J. Hone, Direct Measurement of Strain-Induced Changes in the Band Structure of Carbon Nanotubes, Phys. Rev. Lett. 100 (2008) 136803.
[7] T.F.T. Cerqueira, S. Botti, A. San Miguel, M.A. Marques, Density-functional tight-binding study of the collapse of carbon nanotubes under hydrostatic pressure, Carbon 69 (2014) 355.
[8] M. Hasegawa, K. Nishidate, Radial deformation and stability of single-wall carbon nanotubes under hydrostatic pressure, Phys. Rev. B 74 (2006) 115401–115410.
[9] J.A. Elliott, J. Sandler, A. Windle, R.J. Young, M. Shaffer, Collapse of single-wall carbon nanotubes is diameter dependent, Phys. Rev. Lett. 92 (2004) 095501.
[10] P. Tangney, R.B. Capaz, C.D. Spataru, M.L. Cohen, S.G. Louie, Structural transformations of carbon nanotubes under hydrostatic pressure, Nano Lett 5 (2005) 2268.
[11] Y. Magnin, F. Rondepierre, W. Cui, D.J. Dunstan, A. San-Miguel, Collapse phase diagram of carbon nanotubes with arbitrary number of walls. Collapse modes and macroscopic analog, Carbon 178 (2021) 552–562.
[12] J. Tersoff, R.S. Ruoff, Structural properties of a carbon-nanotube crystal, Phys. Rev. Lett. 73 (1994) 676.
[13] Y.W. Sun, D.G. Papageorgiou, C.J. Humphreys, D.J. Dunstan, P. Puech, J.E. Proctor, C. Bousige, D. Machon, A. San-Miguel, Mechanical properties of graphene, Appl. Phys. Rev. 8 (2021) 021310.
[14] M.J. Peters, L.E. McNeil, J. Lu, D. Kahn, Structural phase transition in carbon nanotube bundles under pressure, Phys. Rev. B 61 (2000) 5939–5944.
[15] U.D. Venkateswaran, A. Rao, E. Richter, M. Menon, A. Rinzler, R.E. Smalley, P. Eklund, Probing the single-wall carbon nanotube bundle: Raman scattering under high pressure, Phys. Rev. B 59 (1999) 10928–10934.
[16] Y. Shen, D. Zerulla, Prediction of the critical point of pressure-induced deformation-related phase transitions in aligned single-walled carbon nanotubes on the basis of extreme-low-frequency-shift Raman spectroscopy, Phys. Rev. B 95 (2017) 205434.
[17] C. Caillier, D. Machon, A. San Miguel, R. Arenal, G. Montagnac, H. Cardon, M. Kalbac, M. Zukalova, L. Kavan, Probing high-pressure properties of single-wall carbon nanotubes through fullerene encapsulation, Phys. Rev. B 77 (2008) 125418.
[18] A.K. Sood, P.V. Teresdesai, D.V. Muthu, R. Sen, A. Govindaraj, C.N.R. Rao, Pressure behaviour of singlewall carbon nanotube bundles and fullerenes: a Raman study, Phys. Stat. Sol. B 215 (1999) 393.
[19] M. Yao, Z. Wang, B. Liu, Y. Zou, S. Yu, W. Lin, Y. Hou, S. Pan, M. Jin, B. Zou, T. Cui, G. Zou, B. Sundqvist, Raman signature to identify the structural transition of single-wall carbon nanotubes under high pressure, Phys. Rev. B 78 (2008) 205411–205419.
[20] Y. Shen, D. Zerulla, Dynamics of the radial deformation recovery process of single-wall carbon nanotubes, Carbon 132 (2018) 466.
[21] M. Yao, S. Lu, J. Xiao, Z. Yao, L. Jiang, T. Cui, B. Liu, Probing factors affecting the Raman modes and structural collapse of single-walled carbon nanotubes under pressure, Phys. Stat. Sol. B 250 (2013) 1370.
[22] S. Sinogeikin, J.S. Smith, E. Rod, C. Lin, C. Kenney-Benson, G. Shen, Online remote control systems for static and dynamic compression and decompression using diamond anvil cells, Rev. Sci. Instrum. 86 (2015) 072209.
[23] W.J. Evans, C.S. Yoo, G.W. Lee, H. Cynn, M.J. Lipp, K. Visbeck, Dynamic diamond anvil cell (dDAC): a novel device for studying the dynamic-pressure properties of materials, Rev. Sci. Instrum. 78 (2007) 073904.
[24] H. Cheng, J. Zhang, Y. Li, G. Li, X. Li, J. Liu, A convenient dynamic loading device for studying kinetics of phase transitions and metastable phases using symmetric diamond anvil cells, High Pressure Res 38 (2018) 32.
[25] J.Y. Chen, C.S. Yoo, High density amorphous ice at room temperature, Proc. Natl. Acad. Sci. 108 (2011) 7685.
[26] C. Lin, J.S. Smith, S. Sinogeikin, G. Shen, Experimental evidence of low-density liquid water upon rapid decompression, Proc. Natl. Acad. Sci. 115 (2018) 2010.
[27] J. Suhr, P. Victor, L. Ci, S. Sreekala, X. Zhang, O. Nalamasu, P. Ajayan, Fatigue resistance of aligned carbon nanotube arrays under cyclic compression, Nat. Nanotechnol. 2 (2007) 417.
[28] S. Pathak, E.J. Lim, P. Abadi, S. Graham, B.A. Cola, J.R. Greer, Higher recovery and better energy dissipation at faster strain rates in carbon nanotube bundles: an in-situ study, ACS Nano 6 (2012) 2189.
[29] G. Ma, Y. Ren, J. Guo, T. Xiao, F. Li, H.M. Cheng, Z. Zhou, K. Liao, How long can single-walled carbon nanotube ropes last under static or dynamic fatigue? Appl. Phys. Lett. 92 (2008) 083105.
[30] R. Zhang, Q. Wen, W. Qian, D.S. Su, Q. Zhang, F. Wei, Superstrong ultralong carbon nanotubes for mechanical energy storage, Adv. Mater. 23 (2011) 3387.
[31] Y. Bai, H. Yue, J. Wang, B. Shen, S. Sun, S. Wang, H. Wang, X. Li, Z. Xu, R. Zhang, F. Wei, Super-durable ultralong carbon nanotubes, Science 369 (2020) 1104–1106.
[32] J. Mu, M.J. Andrade, S. Fang, X. Wang, E. Gao, N. Li, S.H. Kim, H. Wang, C. Hou, Q. Zhang, M. Zhu, D. Qian, H. Lu, D. Kongahage, S. Talebian, J. Foroughi, G.M. Spinks, H. Kim, T. Ware, H.J. Sim, D.Y. Lee, Y. Jang, S. Kim, R.H. Baughman, Sheath-run artificial muscles, Science 365 (2019) 150.
[33] M. Milnera, J. Kurti, M. Hulman, H. Kuzmany, Periodic resonance excitation and intertube interaction from quasicontinuous distributed helicities in single-wall carbon nanotubes, Phys. Rev. Lett. 84 (2000) 1324.
[34] L. Su, K. Shi, L. Zhang, Y. Wang, G. Yang, Static and dynamic diamond anvil cell (s-dDAC): a bidirectional remote controlled device for static and dynamic compression/decompression, Matter Radiat. Extremes 7 (2022) 018401.
[35] C. Bousige, A. Stolz, S. Silva-Santos, J. Shi, W. Cui, C. Nie, M.A. Marques, E. Flahaut, M. Monthioux, A. San-Miguel, Superior carbon nanotube stability by molecular filling:a singlechirality study at extreme pressures, Carbon 183 (2021) 884–892.
[36] M. Krottenmuller, W. Gao, B. Anis, J. Kono, C. Kuntscher, High-pressure optical study of small-diameter chirality-enriched single-wall carbon nanotubes, Phys. Stat. Sol. B 253 (2016) 2446.
[37] A. Merlen, P. Toulemonde, N. Bendiab, A. Aouizerat, J.L. Sauvajol, G. Montagnac, H. Cardon, P. Petit, A. San Miguel, Raman spectroscopy of open-ended single wall carbon nanotubes under pressure: effect of the pressure transmitting medium, Phys. Stat. Sol. B 243 (2006) 690.
[38] A. Merlen, N. Bendiab, P. Toulemonde, A. Aouizerat, A. San Miguel, J.L. Sauvajol, G. Montagnac, H. Cardon, P. Petit, Resonant Raman spectroscopy of single-wall carbon nanotubes under pressure, Phys. Rev. B 72 (2005) 035409-6.
[39] S. Karmakar, S. Sharma, P. Teredesai, D.V. Muthu, A. Govindaraj, S. Sikka, A.K. Sood, Structural changes in single-walled carbon nanotubes under non-hydrostatic pressures: x-ray and Raman studies, New J. Phys. 5 (2003) 143.1.
[40] S. Lu, M. Yao, Q. Li, H. Lv, D. Liu, B. Liu, R. Liu, L. Jiang, Z. Yao, Z. Liu, B. Zou, T. Cui, B. Liu, Exploring the possible interlinked structures in single-wall carbon nanotubes under pressure by Raman spectroscopy, J. Raman Spectrosc. 44 (2013) 176.
[41] K. Thirunavukkuarasu, F. Hennrich, K. Kamaras, C. Kuntscher, Infrared spectroscopic studies on unoriented single-walled carbon nanotube films under hydrostatic pressure, Phys. Rev. B 81 (2010) 045424.
[42] B. Anis, F. Borrnert, M.H. Rummeli, C. Kuntscher, Optical microspectroscopy study of the mechanical stability of empty and filled carbon nanotubes under hydrostatic pressure, J. Phys. Chem. C 118 (2014) 27048.
[43] S. Rols, I.N. Goncharenko, R. Almairac, J.L. Sauvajol, I. Mirebeau, Polygonization of single-wall carbon nanotube bundles under high pressure, Phys. Rev. B 64 (2001) 153401.
[44] S. Reich, C. Thomsen, P. Ordejon, Elastic properties and pressure-induced phase transitions of single-walled carbon nanotubes, Phys. Stat. Sol. B 235 (2003) 354.
[45] S.M. Sharma, S. Karmakar, S. Sikka, P. Teredesai, A.K. Sood, A. Govindaraj, C.N.R. Rao, Pressure-induced phase transformation and structural resilience of single-wall carbon nanotube bundles, Phys. Rev. B 63 (2001) 205417.
[46] A.C. Torres-Dias, S. Cambre, W. Wenseleers, D. Machon, A. San Miguel, Chirality-dependent mechanical response of empty and water-filled single-wall carbon nanotubes at high pressure, Carbon 95 (2015) 442.

[47] S. Lebedkin, K. Arnold, O. Kiowski, F. Hennrich, M. Kappes, Raman study of individually dispersed single-walled carbon nanotubes under pressure, Phys. Rev. B 73 (2006) 094109.
[48] M. Mases, V. Milyavskiy, J. Waldbock, M. Dossot, X. Devaux, M. McRae, A. Soldatov, The effect of shock wave compression on double wall carbon nanotubes, Phys. Stat. Sol. B 12 (2012) 2378–2381.
[49] J.A. Xu, H.K. Mao, Moissanite: a window for high-pressure experiments, Science 290 (2000) 783.
[50] M.S. Amer, M.M. El-Ashry, J.F. Maguire, Study of the hydrostatic pressure dependence of the Raman spectrum of single-walled carbon nanotubes and nanospheres, J. Chem. Phys. 121 (2004) 2752.
[51] J.E. Proctor, M.P. Halsall, A. Ghandour, D.J. Dunstan, Effect of chemical environment on high-pressure Raman response of single-walled carbon nanotubes, High Pressure Res 26 (2006) 335–339.
[52] J.E. Proctor, M.P. Halsall, A. Ghandour, D.J. Dunstan, High pressure Raman spectroscopy of single-walled carbon nanotubes: effect of chemical environment on individual nanotubes and the nanotube bundle, J. Phys. Chem. Solids 67 (2006) 2468–2472.
[53] J.E. Proctor, M.P. Halsall, A. Ghandour, D.J. Dunstan, Raman spectroscopy of single-walled carbon nanotubes at high pressure: effect of interactions between the nanotubes and pressure transmitting media, Phys. Stat. Sol. B 244 (2007) 147–150.
[54] H. Honda, C.M. Yang, H. Kanoh, H. Tanaka, T. Ohba, Y. Hattori, S. Utsumi, K. Kaneko, Choking effect of single-wall carbon nanotubes on solvent adsorption in radial breathing mode, J. Phys. Chem. C 111 (2007) 3220–3223.
[55] K. Gao, R.C. Dai, Z. Zhao, Z.M. Zhang, Z.J. Ding, Effects of pressure transmitting media on Raman features of single-walled carbon nanotubes, Solid State Commun 147 (2008) 65–68.
[56] M.J. Longhurst, N. Quirke, Pressure dependence of the radial breathing mode of carbon nanotubes: the effect of fluid adsorption, Phys. Rev. Lett. 98 (2007) 145503.
[57] A. Abouelsayed, K. Thirunavukkuarasu, F. Hennrich, C. Kuntscher, Role of the pressure transmitting medium for the pressure effects in single-walled carbon nanotubes, J. Phys. Chem. C 114 (2010) 4424–4428.
[58] J.R. Xiao, S.L. Lopatnikov, B.A. Gama, J.W. Gillespie, Nanomechanics on the deformation of single- and multi-walled carbon nanotubes under radial pressure, Mater. Sci. Eng. A 416 (1–2) (2006) 192–204.
[59] S.P. Chan, W.L. Yim, X.G. Gong, Z.F. Liu, Carbon nanotube bundles under high pressure:transformation to low-symmetry structures, Phys. Rev. B 68 (2003) 075404–075407.
[60] A. Bosak, M. Krisch, M. Mohr, J. Maultzsch, C. Thomsen, Elasticity of single-crystalline graphite: inelastic x-ray scattering study, Phys. Rev. B 75 (2007) 153408.
[61] J. Tang, L.C. Qin, T. Sasaki, M. Yudasaka, A. Matsushita, S. Iijima, Compressibility and polygonization of single-walled carbon nanotubes under hydrostatic pressure, Phys. Rev. Lett. 85 (2000) 1887.
[62] M.F. Ashby, Materials Selection in Mechanical Design, Butterworth-Heinemann, Oxford, UK, 2005.
[63] G. Grimvall, Thermophysical Properties of Materials, Amsterdam, North-Holland, 1986.
[64] J. Proctor, E. Gregoryanz, K.S. Novoselov, M. Lotya, J.N. Coleman, M.P. Halsall, High-pressure Raman spectroscopy of graphene, Phys. Rev. B 80 (2009) 073408-4.
[65] M. Hanfland, H. Beister, K. Syassen, Graphtie under pressure: equation of state and first-order Raman modes, Phys. Rev. B 39 (1989) 12598.
[66] R. Zallen, Pressure-Raman effects and vibrational scaling laws in molecular crystals: S_8 and As_2S_3, Phys. Rev. B 9 (10) (1974) 4485–4496.
[67] P. Teredesai, A.K. Sood, D.V. Muthu, R. Sen, A. Govindaraj, C.N.R. Rao, Pressure-induced reversible transformation in single-wall carbon nanotube bundles studied by Raman spectroscopy, Chem. Phys. Lett. 319 (2000) 296.
[68] V.N. Popov, V.E. Van Doren, M. Balkanski, Elastic properties of crystals of single-walled carbon nanotubes, Solid State Commun 114 (2000) 395–399.
[69] J.P. Lu, Elastic properties of carbon nanotubes and nanoropes, Phys. Rev. Lett. 79 (1997) 1297.
[70] S. Reich, C. Thomsen, P. Ordejon, Elastic properties of carbon nanotubes under hydrostatic pressure, Phys. Rev. B 65 (2002) 153407-4.
[71] W. Lu, T.W. Chou, B.S. Kim, Radial deformation and its related energy variations of single-walled carbon nanotubes, Phys. Rev. B 83 (13) (2011) 134113.
[72] A.C. Ferrari, J. Robertson, Raman Spectroscopy in carbons: from Nanotubes to Diamond, The Royal Society, London, 2004.
[73] M. Damnjanovic, I. Milosevic, T. Vukovic, R. Sredanovic, Full symmetry, optical activity, and potentials of single-wall and multiwall nanotubes, Phys. Rev. B 60 (1999) 2728–2739.
[74] J.F. Nye, Physical Properties of Crystals: Their Representation By Tensors and Matrices, Oxford University Press, England, 1985.
[75] S. Reich, H. Jantoljak, C. Thomsen, Shear strain in carbon nanotubes under hydrostatic pressure, Phys. Rev. B 61 (2000) R13389–R13392.
[76] F. Cerdeira, C.J. Buchenauer, F.H. Pollak, M. Cardona, Stress-induced shifts of first-order raman frequencies of diamond- and zinc-blende-type semiconductors, Phys. Rev. B 5 (1972) 580–593.
[77] H. Sakata, G. Dresselhaus, M.S. Dresselhaus, M. Endo, Effect of uniaxial stress on the Raman spectra of graphite fibers, J. Appl. Phys. 63 (1988) 2769.
[78] X. Chen, H. Lou, Z. Zeng, B. Cheng, X. Zhang, Y. Liu, D. Xu, K. Yang, Q. Zeng, Structural transitions of 4:1 methanol–ethanol mixture and silicone oil under high pressure, Matter Radiat. Extremes 6 (2021) 038402.
[79] J.C. Jamieson, Crystal structures at high pressures of metallic modifications of silicon and germanium, Science 139 (1963) 762–764.
[80] S. Minomura, H.G. Drickamer, Pressure induced phase transitions in silicon, germanium and some III-V compounds, J. Phys. Chem. Solids 23 (1962) 451–456.